Comparisons of methods for evaluating mechanical stress in the rotor of high-speed machines

Larbi Dahnoun, Thomas Marcand, Rachid Rahouadj, Cédric P. Laurent, Benjamin Dagusé, Charles-Henri Bonnard, Julien Fontchastagner, Smail Mezani, Noureddine Takorabet

Comparisons of methods for evaluating mechanical stress in the rotor of high-speed machines

L. Dahnoun, T. Marcand, R. Rahouadj, C. Laurent, B. Daguse,
C-H. Bonnard, J. Fontchastagner, S. Mezani, N. Takorabet

***Abstract* -- High-speed rotating electrical machines are interesting solutions to achieve high-power density, especially in transportation industry. Such machines are considered as high-speed ones when the mechanical aspects like stress and vibrations cannot anymore be neglected during their sizing. Machine topologies having a solid rotor (homopolar, reluctance and asynchronous) are suited to high speed operation. Permanent magnet machines can also operate at high-speed if they are properly sized. This paper proposes analytical evaluation of the stresses in the rotor caused by the centrifugal effects in order to determine the speed limit, ensuring a mechanical sizing of the rotating parts of both solid rotor and permanent magnet machines which will operate in their elastic regime. Comparisons of the developed models with simulations using finite element method as well as retro-engineering on industrial applications serve to validate and analyze the analytical findings.**

***Index Terms*-- Centrifugal effect, electrical machine design, high-speed, permanent magnet, solid rotor, stress**

I. Nomenclature

$\underline{\underline{\sigma}}$	Stress tensor
$\rho_{ac,a,f}$	Density of steel, magnet or bandage
$\underline{f}$	Volumic forces
$\underline{\underline{\epsilon}}$	Strain tensor
$E_{ac,a,f}$	Young's modulus of steel, magnet or bandage
$\vartheta_{ac,a,f}$	Poisson's ratio of stell, magnet or bandage
ω	Angular velocity
v	Linear velocity
σ_{VM}	Von Mises's stress
σ_T	Tresca's stress
R_i	Inner radius of the solid rotor
R_e	Outer radius of the solid rotor
$\underline{u}$	Field displacement
$\lambda_{ac,a,f}$	Lamé's parameters of steel, magnet or bandage
$\mu_{ac,a,f}$	Lamé's parameters of steel, magnet or bandage
P_1	Pression between steel and magnet
P_2	Pression between magnet and bandage
P_2'	Pression's composition
$R_{int}^{(1)}$	Inner radius of steel of PMSM rotor
$R_{ext}^{(1)}$	Outer radius of steel of PMSM rotor
$R_{int}^{(2)}$	Inner radius of magnet of PMSM rotor
$R_{ext}^{(2)}$	Outer radius of magnet of PMSM rotor
$R_{int}^{(3)}$	Inner radius of bandage of PMSM rotor
$R_{ext}^{(3)}$	Inner radius of bandage of PMSM rotor
e	Mechanical interferences
e_f	Sleeve's thickness
$\underline{\underline{\sigma_{tot}}}$	Stress tensor of the total's stresses
$\underline{\underline{\sigma_{prestress}}}$	Stress tensor of the prestress
$\underline{\underline{\sigma_{centri}}}$	Stress tensor of the centrifugal effect
p_i	Pressure at the interface magnet/bandage

II. Introduction

TRANSPORTATION electrification requires greater energy needs as well as higher power densities, particularly in the avionic and aerospace industries. High-speed motors and generators allow higher power density levels in many applications like [1]:

- Compressors or vacuum pumps
- Generators for aircraft engine
- Milling machines

The overall mass of the system can thus be reduced while mechanical gears are removed which reduces maintenance, manufacturing cost and increases system reliability.

Several machine topologies are suitable for high-speed applications among which solid rotors or squirrel cage induction motors, homopolar synchronous machines and permanent magnet synchronous machines (PMSM) are the most used. Note that PMSMs have the advantage of drastically reduce rotor losses.

High speed machines are subjected to significant mechanical stresses due to centrifugal effects and therefore their sizing require a particular attention. This results in an important interaction with the electromagnetic sizing because some geometric parameters influence both electromagnetic and mechanical aspects [1]-[4].

In this article, the authors present detailed analytical models to predict mechanical response of a rotor subjected to centrifugal effects, then results are compared to numerical calculations.

The entire study is achieved in cylindrical coordinates (r, θ, z) while both solid and hollow configurations are

L. Dahnoun, T. Marcand, C-H. Bonnard, J. Fontchastagner, S. Mezani and N. Takorabet are with GREEN, Université de Lorraine, F-54000 Nancy, FRANCE (e-mail : larbi.dahnoun@univ-lorraine.fr, thomas.marcand@univ-lorraine.fr, charles-henri.bonnard@univ-lorraine.fr, julien.fontchastagner@univ-lorraine.fr, smail.mezani@univ-lorraine.fr, noureddine.takorabet@univ-lorraine.fr)

R. Rahouadj and C. Laurent are with Laboratoire LEM3 UMR CNRS 7239, 7 Rue Félix Savart, 57070 Metz, FRANCE (e-mail : rachid.rahouadj@univ-lorraine.fr, cedric.laurent@univ-lorraine.fr)

L. Dahnoun and B. Daguse are with Electrical and Electronic Systems Research Group, Safran Tech, F-78114 Magny-Les-Hameaux, FRANCE (e-mail: larbi.dahnoun@safrangroup.com, benjamin.daguse@safrangroup.com)

considered. The materials that are used are all assumed to have linear elastic and isotropic properties.

III. Analytical Modeling of a Thin Disk

For the study of a rotating thin disk, only plane stresses (tangential and radial) with radial displacement are considered. By exploiting the axisymmetry of the rotating disk, the components of our variables are independent of the coordinate θ and we also assume that there are no forces at the internal surface (perfect mechanical clearance between the disk and the shaft) and at the external one (no aeraulic effect). Thus, in the cylindrical coordinate system linked to the disk we can write the following equilibrium equation:

$$\underline{div}\left(\underline{\underline{\sigma}}\right) + \rho \underline{f} = \underline{0} \quad (1)$$

With $\underline{\underline{\sigma}}$ the second-order Cauchy stress tensor in the disk.
ρ the density of the material.
$\underline{f}$ the vector symbolizing the volume forces induced by the rotational speed that can be written as $\underline{f} = r\omega^2 \underline{e_r}$.

Within the framework of our model and the simplifications it implies, we can write the matrix of stress components $\underline{\underline{\sigma}}$ as well as the strain tensor $\underline{\underline{\epsilon}}$ under the small displacement approximation:

$$\left[\underline{\underline{\sigma}}\right] = \begin{bmatrix} \sigma_{rr}(r) & 0 & 0 \\ 0 & \sigma_{\theta\theta}(r) & 0 \\ 0 & 0 & 0 \end{bmatrix} \text{ and } \epsilon_{rr} - \epsilon_{\theta\theta} = r\frac{\partial \epsilon_{\theta\theta}}{\partial r} \quad (2)$$

The material constitutive law introduces the Young modulus E and the Poisson coefficient ϑ which lead to:

$$\underline{\underline{\epsilon}} = \frac{1+\vartheta}{E}\underline{\underline{\sigma}} - \frac{\vartheta}{E} Tr\left(\underline{\underline{\sigma}}\right)\underline{\underline{I}} \Rightarrow \begin{cases} \epsilon_{rr} = \dfrac{\sigma_{rr}}{E} - \dfrac{\vartheta\sigma_{\theta\theta}}{E} \\ \epsilon_{\theta\theta} = \dfrac{\sigma_{\theta\theta}}{E} - \dfrac{\vartheta\sigma_{rr}}{E} \end{cases} \quad (3)$$

Finally, we have the system of equation and the following solutions:

$$\begin{cases} \frac{\partial \sigma_{rr}}{\partial r} + \frac{\sigma_{rr} - \sigma_{\theta\theta}}{r} + \rho\omega^2 r = 0 \\ (1+\vartheta)(\sigma_{rr} - \sigma_{\theta\theta}) = r\left(\frac{\partial \sigma_{\theta\theta}}{\partial r} - \vartheta\frac{\partial \sigma_{rr}}{\partial r}\right) \end{cases} \Rightarrow$$

$$\begin{cases} \sigma_{rr}(r) = \dfrac{-\rho\omega^2(3+\vartheta)}{8} r^2 - \dfrac{A}{2r^2} + B \\ \sigma_{\theta\theta}(r) = \dfrac{-\rho\omega^2(1+3\vartheta)}{8} r^2 + \dfrac{A}{2r^2} + B \end{cases} \quad (4)$$

Where A and B are constants determined by the boundary conditions.

A. Plasticity criteria

Analytical models allow to identify the different stresses within the materials. In order to compare the computed mechanical stresses with the material yield strength, an equivalent stress must be formulated. To do so, one has to choose among the various yield criteria used in the literature. In this work, we use Von Mises (σ_{VM}) or Tresca (σ_T) equivalent stresses that are the most common for isotropic metallic materials. These criteria determine the limit of the elastic linear regime of the material. In order to avoid the transition to plastic state, these criteria must be lower than the yield strength of the material. These conditions are given by equation (5).

$$\sigma_{VM} = \frac{1}{\sqrt{2}}\sqrt{(\sigma_I - \sigma_{II})^2 + (\sigma_{II} - \sigma_{III})^2 + (\sigma_{III} - \sigma_I)^2} \leq \sigma_e$$
$$\text{or } \sigma_T = \max(|\sigma_I - \sigma_{II}|, |\sigma_{II} - \sigma_{III}|, |\sigma_I - \sigma_{III}|) \leq \sigma_e \quad (5)$$

B. Application to the solid rotor

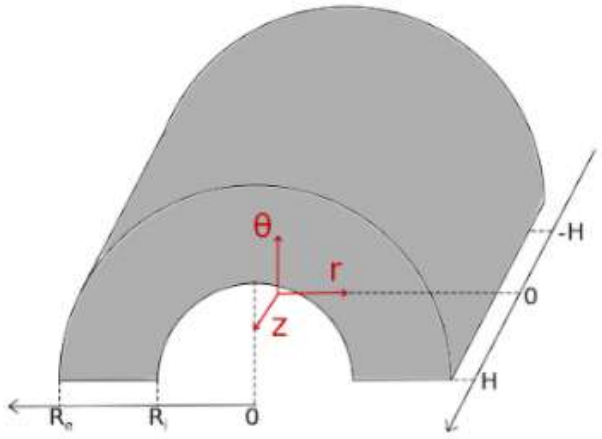

Fig. 1. Simplified geometry of the solid rotor

As depicted in Fig. 1., R_i and R_e represent the inner and outer radii of the disk, respectively. In the case of a hollow cylinder, the boundary conditions consist of setting a null radial stress on both $r = R_i$ and $r = R_e$. For the solid cylinder, a zero stress is imposed on $r = R_e$ and a maximum stress is imposed at $r = R_i = 0$. Table 1 summarizes the analytical expressions of the stresses for the hollow and solid cases.

TABLE I
Expressions of Plane Stresses in a Rotating Thin Disk

Hollow disk	$\begin{cases} \sigma_{rr}(r) = \frac{-\rho\omega^2(3+\vartheta)}{8r^2}(r^2 - R_i^2)(r^2 - R_e^2) \\ \sigma_{\theta\theta}(r) = \frac{\rho\omega^2}{8} r^2 \left[(3+\vartheta)\left(\frac{R_i^2 R_e^2}{r^4} + \frac{R_i^2 + R_e^2}{r^2}\right) - (1+3\vartheta)\right] \end{cases}$
Solid disk	$\begin{cases} \sigma_{rr}(r) = \dfrac{\rho\omega^2(3+\vartheta)}{8}\left({R_e}^2 - r^2\right) \\ \sigma_{\theta\theta}(r) = \dfrac{\rho\omega^2}{8}\left((3+\vartheta){R_e}^2 - (1+3\vartheta)r^2\right) \end{cases}$

It can be seen that in the case of a hollow disk, the maximum radial stress is reached at $\sqrt{R_i R_e}$ and that $max(|\sigma_I - \sigma_{II}|, |\sigma_{II} - \sigma_{III}|, |\sigma_I - \sigma_{III}|) = \sigma_{\theta\theta max} = \frac{3+\vartheta}{4}\left(1 + \frac{1-\vartheta}{3+\vartheta}\frac{{R_i}^2}{{R_e}^2}\right)\rho v^2$ whereas for a solid disk the constraints are maximum at $r = 0$ and $\sigma_{\theta max} = \sigma_{r max} = \frac{3+\vartheta}{8}\rho v^2$.

Thus, these results show that in both studied cases, the maximum stress of Tresca are reached at the center of the material, it is then preferable to fix half shafts on either side of the rotating disk rather than perforating it since the stress in the latter case is at least twice as great.

To complete the study two other analytical models have been developed. The first one uses the same planar stresses but includes an axial dependency. Thus, we are reconsidering the stress matrix as follows:

$$[\underline{\sigma}] = \begin{bmatrix} \sigma_{rr}(r,z) & 0 & 0 \\ 0 & \sigma_{\theta\theta}(r,z) & 0 \\ 0 & 0 & 0 \end{bmatrix} (6)$$

Using (1), (2) and (3) leads to these expressions where $A(z)$ and $B(z)$ are variables depending only on z that are further determined:

$$\begin{cases} \sigma_{rr}(r,z) = \dfrac{-\rho\omega^2(3+\vartheta)}{8} r^2 - \dfrac{A(z)}{2r^2} + B(z) \\ \sigma_{\theta\theta}(r,z) = \dfrac{-\rho\omega^2(1+3\vartheta)}{8} r^2 + \dfrac{A(z)}{2r^2} + B(z) \end{cases} (7)$$

Afterwards we use the hypothesis of our model which claims that we have no shearing effects ($\sigma_{rz} = 0$). Also, we consider that, regarding the symmetry of the geometry, $u_z(r,0) = 0$. Using the same boundary conditions as in section III.B but with the resultants of the stresses we obtain:

TABLE II
EXPRESSIONS OF PLANE STRESSES DEPENDING ON RADIAL AND AXIAL POSITION IN A ROTATING THIN DISK

Hollow disk	$\begin{cases} \sigma_{rr}(r,z) = \frac{-\rho\omega^2(3+\vartheta)}{8r^2}\left(r^2 - {R_i}^2\right)\left(r^2 - {R_e}^2\right) + \frac{\rho\omega^2\vartheta(1+\vartheta)}{2(1-\vartheta)}\left(\frac{H^2}{3} - z^2\right) \\ \sigma_{\theta\theta}(r,z) = \frac{-\rho\omega^2}{8r^2}\left[(1+3\vartheta)r^4 - (3+\vartheta)\left(\left({R_i}^2 + {R_e}^2\right)r^2 + {R_i}^2{R_e}^2\right)\right. \\ \left. + \frac{\rho\omega^2\vartheta(1+\vartheta)}{2(1-\vartheta)}\left(\frac{H^2}{3} - z^2\right)\right) \end{cases}$
Solid disk	$\begin{cases} \sigma_{rr}(r,z) = \frac{-\rho\omega^2(3+\vartheta)}{8}\left(r^2 - {R_e}^2\right) + \frac{\rho\omega^2\vartheta(1+\vartheta)}{2(1-\vartheta)}\left(\frac{H^2}{3} - z^2\right) \\ \sigma_{\theta\theta}(r,z) = \frac{\rho\omega^2}{8}\left[(3+\vartheta){R_e}^2 - (1+3\vartheta)r^2\right] + \frac{\rho\omega^2\vartheta(1+\vartheta)}{2(1-\vartheta)}\left(\frac{H^2}{3} - z^2\right) \end{cases}$

Notice that to obtain these analytical expressions we have done several hypotheses which are correct only under the assumption $H/r \ll 1$.

Finally, we also develop a third analytical model leading to a 3D stress matrix. This model is more representative of a rotating cylinder as the axial stress can more easily develop itself in the matter. Starting from a displacement method claiming that we only have an axial and radial displacement of the matter we have:

$$\underline{u} = u_r(r)\underline{e_r} + u_z(z)\underline{e_z} \Rightarrow [\epsilon] = \begin{bmatrix} \frac{\partial u_r}{\partial r} & 0 & 0 \\ 0 & \frac{u_r}{r} & 0 \\ 0 & 0 & \frac{\partial u_z}{\partial z} \end{bmatrix}$$

$$\Rightarrow \begin{cases} \sigma_{rr} = (\lambda+2\mu)\dfrac{\partial u_r}{\partial r} + \lambda\left(\dfrac{u_r}{r} + \epsilon_{zz}\right) \\ \sigma_{\theta\theta} = (\lambda+2\mu)\dfrac{u_r}{r} + \lambda\left(\dfrac{\partial u_r}{\partial r} + \epsilon_{zz}\right) \\ \sigma_{zz} = (\lambda+2\mu)\epsilon_{zz} + \lambda\left(\dfrac{\partial u_r}{\partial r} + \dfrac{u_r}{r}\right) \end{cases} (8)$$

$$\text{(1) equation leads to } \begin{cases} \frac{\partial \sigma_{rr}}{\partial r} + \frac{\sigma_{rr} - \sigma_{\theta\theta}}{r} + \rho\omega^2 r = 0 \\ \frac{\partial \sigma_{zz}}{\partial z} = 0 \end{cases} (9)$$

Finally, we obtain the analytical expressions of u_r and u_z where K_1, K_2 and K_3 are constants which are defined thanks to boundaries conditions:

$$\begin{cases} u_r(r) = -\dfrac{\rho\omega^2}{8(\lambda+2\mu)} r^3 + K_1 r + \dfrac{K_2}{r} \\ u_z(z) = K_3 z \end{cases} (10)$$

For example, in the case of a solid disk the radial stress is null on the external surface of the rotor as no efforts are exerted as well as the resultant of the axial stress on either side of the rotor. This configuration leads to $K_1 = \frac{\rho\omega^2{R_e}^2}{8E}\frac{3-5\vartheta}{1-\vartheta}$, $K_2 = 0$ and $K_3 = \frac{-\rho\omega^2{R_e}^2}{2}\frac{\vartheta}{E}$. Thus, the stresses can be easily expressed as following:

$$\begin{cases} \sigma_{rr} = \dfrac{\rho v^2}{8}\dfrac{3-2\vartheta}{1-\vartheta}\left(1 - \dfrac{r^2}{{R_e}^2}\right) \\ \sigma_{\theta\theta} = \dfrac{\rho v^2}{8(1-\vartheta)}\left((3-2\vartheta) - (1+2\vartheta)\dfrac{r^2}{{R_e}^2}\right) \\ \sigma_{zz} = \dfrac{\rho v^2}{4}\dfrac{\vartheta}{1-\vartheta}\left(1 - 2\dfrac{r^2}{{R_e}^2}\right) \end{cases} (11)$$

This analytical result shows that unlikely to the Poisson's ratio, the Young's modulus of the rotor material has no effect on the mechanical handling. Moreover, all the three stresses are maximum at the center of the matter and are equal to:

$$\begin{cases} \sigma_{rrmax} = \sigma_{\theta\theta max} = \dfrac{3-2\vartheta}{8(1-\vartheta)}\rho v^2 \\ \sigma_{zzmax} = \dfrac{\vartheta}{4(1-\vartheta)}\rho v^2 \end{cases} (12)$$

Thanks to the expression of the maximal stresses in the 2D model depending only on r and the 3D one we can express the Von Mises criteria at the center of the matter:

$$\sigma_{VM2D} = \frac{3+\vartheta}{8}\rho v^2 \text{ and } \sigma_{VM3D} = \frac{1}{8}\left(\frac{3-4\vartheta}{1-\vartheta}\right)\rho v^2 \quad (13)$$

Indeed, for a material with a Poisson's ratio of 0.3 we have $\sigma_{VM2D} = 0.413\rho v^2$ whereas $\sigma_{VM3D} = 0.321\rho v^2$ explaining the fact that mechanical handling is easier to obtain in a cylinder than in a disk as the speed limit of the former is, in this case, 13% higher than the latter.

C. Application to PMSM

The study carried out previously can be applied to PMSM. High-speed PMSM requires a sleeve to hold the magnets on the rotor yoke. This enclosure cannot be ferromagnetic, and it must have a low mass density as well as a high yield strenght. Indeed, it is this part of the machine which ensure the mechanical handling of the overall rotating system. Thus in this part, the mechanical study focuses on the stresses in the sleeve. In [1], authors select glass-fiber or carbon-fiber for the bandage. It is specified that the use of carbon-fiber is preferred when the circumferential speeds are above 150 m/s because glass-fiber bandages are unlikely to ensure safe fixation between the magnets and the rotor surface. However, in this contribution and for the sake of simplicity, we focus on the glass-fiber because of their nearly isotropic characteristics due to random fiber orientations.

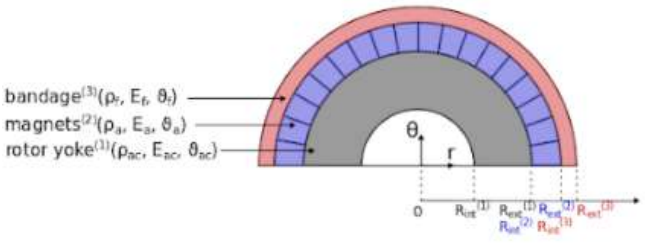

Fig. 2. Simplified geometry of PMSM rotor considering 3 different layers.

The mechanical analytical model of this rotor is based on three concentric cylinders. Each one is modeled by the approach previously detailed and numbered respectively from 1 to 3 starting from the rotor yoke to the bandage. As multi-layer topology is considered, boundary conditions need to be implemented in the model.

The use of bandage allows to maintain the contact between the magnets and the yoke as well as between the sleeve and the magnets. At the interface between the materials, the displacement field is considered to be continuous and the principle of reaction-action is applied. The system (14) represents these boundary conditions.

$$\begin{cases} u_{rext1}^{(1)} = u_{rint2}^{(2)} \\ u_{rext2}^{(2)} = u_{rint3}^{(3)} \\ \underline{t}\left(r = r_{ext1}^{(1)}, \underline{n} = \underline{e_r}\right) = -\underline{t}\left(r = r_{in}^{(2)}, \underline{n} = -\underline{e_r}\right) \\ \underline{t}\left(r = r_{ext2}^{(2)}, \underline{n} = \underline{e_r}\right) = -\underline{t}\left(r = r_{int3}^{(3)}, \underline{n} = -\underline{e_r}\right) \end{cases} \Rightarrow \begin{cases} u_{rext1}^{(1)} = u_{rint2}^{(2)} \\ u_{rext2}^{(2)} = u_{rint3}^{(3)} \\ \sigma_{rr}^{(1)}\left(r = r_{ext1}^{(1)}\right) = \sigma_{rr}^{(2)}\left(r = r_{int2}^{(2)}\right) \\ \sigma_{rr}^{(2)}\left(r = r_{ext2}^{(2)}\right) = \sigma_{rr}^{(3)}\left(r = r_{int3}^{(3)}\right) \end{cases} \quad (14)$$

Considering such boundary conditions, one can determine stresses within each material and pressures required at each interface to ensure the contact between the different components. These pressures consist in mechanical interferences between the cylinders respectively named P_1 and P_2 for the pressure at the rotor yoke/magnet interface and magnet/sleeve one. However, only the bandage is really prestressed, so we must calculate the necessary pression P_2' at the magnet/sleeve interface to maintain each cylinder in contact and reach the pressures previously calculated. P_2' is calculated from the thin-shell hypothesis using equation (15).

$$P_2' = P_2 + P_1 \frac{R_{int}^{(2)}}{R_{ext}^{(2)}} \quad (15)$$

A second method which is called displacement method [5] consists in calculating the displacement of all the cylinders subjected to the centrifugal effect. Displacement calculation allows to determine mechanical interference between each cylinder. To identify these interferences, four displacements must be calculated: 1) the displacement of the outer radius of the rotor yoke, 2) & 3) the displacement of the inner and outer radii of the magnet and 4) the displacement of the inner radius of the sleeve. System (16) represents the different displacements.

$$\begin{cases} u^{(1)}\left(r = R_{ext}^{(1)}\right) = \frac{2.(3+\vartheta_{ac}).\rho_{ac}.\omega^2.R_{ext}^{(1)\,3}}{8.E_{ac}}.\left(\frac{1-\vartheta_{ac}}{3+\vartheta_{ac}} + \left(\frac{R_{int}^{(1)}}{R_{ext}^{(1)}}\right)^2\right) \\ u^{(2)}\left(r = R_{int}^{(2)}\right) = \frac{2.(3+\vartheta_a).\rho_a.\omega^2.R_{ext}^{(2)\,2}.R_{int}^{(2)}}{8.E_a}.\left(1 + \frac{1-\vartheta_a}{3+\vartheta_a}.\left(\frac{R_{int}^{(2)}}{R_{ext}^{(2)}}\right)^2\right) \\ u^{(2)}\left(r = R_{ext}^{(2)}\right) = \frac{2.(3+\vartheta_a).\rho_a.\omega^2.R_{ext}^{(2)\,3}}{8.E_a}.\left(\frac{1-\vartheta_a}{3+\vartheta_a} + \left(\frac{R_{int}^{(2)}}{R_{ext}^{(2)}}\right)^2\right) \\ u^{(3)}\left(r = R_{int}^{(3)}\right) = \frac{2.(3+\vartheta_f).\rho_f.\omega^2.R_{ext}^{(3)\,2}.R_{int}^{(3)}}{8.E_f}.\left(1 + \frac{1-\vartheta_f}{3+\vartheta_f}.\left(\frac{R_{int}^{(3)}}{R_{ext}^{(3)}}\right)^2\right) \end{cases} \quad (16)$$

Using these expressions, one can identify two mechanical interferences, between the rotor yoke and the magnet as well as between the magnet and the bandage. These values allow to determine the necessary interferences to keep the different cylinders in contact.

$$\begin{cases} e^{(1,2)} = u^{(2)}\left(r = R_{int}^{(2)}\right) - u^{(1)}\left(r = R_{ext}^{(1)}\right) \\ e^{(2,3)} = u^{(3)}\left(r = R_{int}^{(3)}\right) - u^{(2)}\left(r = R_{ext}^{(2)}\right) \end{cases} \quad (17)$$

With these values, one can determine pressure at the boundaries of each material. As previously used, only the bandage is really prestressed, so we must finally calculate the required pressure between the magnet and the sleeve to maintain each cylinder in contact. Once done, one can calculate the mechanical interference between the magnet and the bandage and also the stresses in the sleeve. These are given by equations (18). The stresses are expressed at the inner radius where they are at their maximum value.

$$\begin{cases} \sigma_{rr}\left(r = R_{int}^{(3)}\right) = -p_2' \\ \sigma_{\theta\theta}\left(r = R_{int}^{(3)}\right) = \frac{(3+\vartheta_f)}{8}.\rho_f.\omega^2.\left(R_{int}^{(3)^2}\left(1 - \frac{1+3.\vartheta_f}{3+\vartheta_f}\right) + 2.R_{ext}^{(3)^2}\right) \\ \qquad -p_2'\left(1 + 2.\frac{R_{ext}^{(3)^2}}{R_{int}^{(3)^2} - R_{ext}^{(3)^2}}\right) \end{cases} \quad (18)$$

A final model has been developed. We consider two separate studies, then we apply the principle of superposition. The equation (19) shows this principle.

$$\underline{\underline{\sigma_{tot}}} = \underline{\underline{\sigma_{prestress}}} + \underline{\underline{\sigma_{centri}}} \tag{19}$$

The stresses caused by the centrifugal effect can be determined with the first model by cancelling the pressures p_1 and p_2. To identify the prestress, we use the mechanical interference found with the displacement method then we calculate the pressure at the interface between magnet and sleeve with the equation (20).

$$p_i = \frac{e}{R_{int}^{(3)} \cdot \left(\frac{1}{E_f} \cdot \left(\frac{{R_{ext}^{(3)}}^2 + {R_{int}^{(3)}}^2}{{R_{ext}^{(3)}}^2 - {R_{int}^{(3)}}^2} + \vartheta_f \right) + \frac{1}{E_a} \cdot \left(\frac{{R_{int}^{(3)}}^2 + {R_{int}^{(2)}}^2}{{R_{int}^{(3)}}^2 - {R_{int}^{(2)}}^2} - \vartheta_i \right) \right)} \tag{20}$$

Using this result, we can calculate the stresses in a cylinder subjected to an internal pressure with the equations (21).

$$\begin{cases} \sigma_{prestress,rr} = \dfrac{{R_{int}^{(3)}}^2 . p_i}{{R_{ext}^{(3)}}^2 - {R_{int}^{(3)}}^2} \cdot \left(1 - \dfrac{{R_{ext}^{(3)}}^2}{r^2} \right) \\ \sigma_{prestress,\theta\theta} = \dfrac{{R_{int}^{(3)}}^2 . p_i}{{R_{ext}^{(3)}}^2 - {R_{int}^{(3)}}^2} \cdot \left(1 + \dfrac{{R_{ext}^{(3)}}^2}{r^2} \right) \end{cases} \tag{21}$$

Using the two tensors, we can obtain the total stresses in the bandage.

IV. Results and Analysis

A. Application to the solid rotor

The proposed analytical models are now used to simulate the stress within a hollow disk and a solid one. In order to compare the models with numerical values, a solid steel disk with a rotation speed of 30,000 rpm has been considered, with an inner bore $R_i = 24.2$ mm , an external radius $R_e = 65.7$ mm and a thickness of 50 mm. The results are plotted for an axial position $z = 1$ mm corresponding at a point localized inside the disk.

Results from the 2D and 3D finite element simulation have been respectively obtained with a 2D and 3D representation of the rotor with a triangle mesh (2D) and tetrahedrons (3D) to avoid hourglass modes on ABAQUS. The size of mesh elements is chosen to obtain at least twenty elements in the diameter or thickness of the disk.

At location $x = 0$ and $y = 0$, we impose a zero displacement in x and y-direction respectively. This prevents the movement of solid bodies. Considering the 3D finite element simulation, we impose a zero displacement in the z-direction at location $z = H$ and $z = -H$ for the same reason as previously and thanks here to the principle of Saint-Venant.

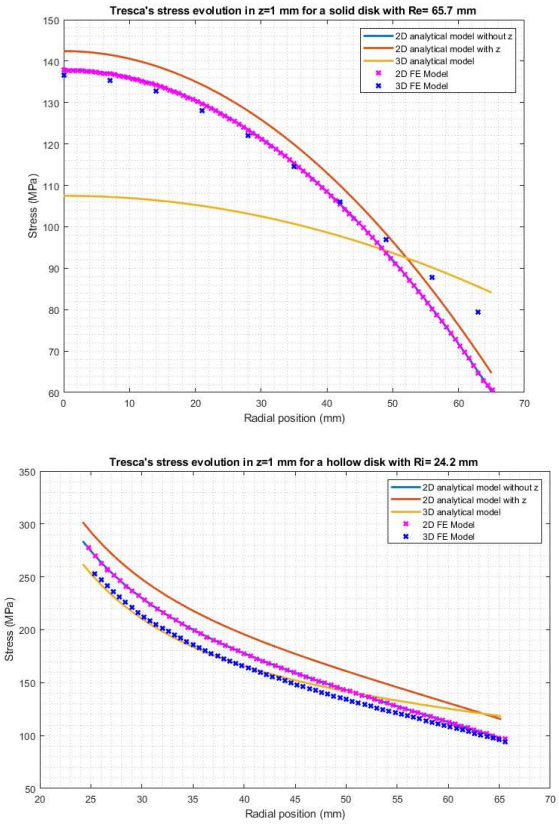

Fig. 3. Stress analysis of a high-speed rotor considering solid (top) and hollow (bottom) disk.

For all the studied cases, we can see that the calculated stresses are lower than the yield strength of the steel σy=400 MPa which corresponds to the elasticity limit of the used material. This is very important because it is this stress limit which allows to determine the speed limit of our rotor.

The results issued from the presented models are almost similar despite their different level of complexity. Moreover, the 2D finite element analysis returns exactly the same results as the planar model considering only radial variation whereas the 3D finite element analysis suits our three-dimensional analytical model only in the hollow disk case. This can be explained by the hypothesis made which are no longer available in the solid disk case.

One can observe that the consideration of 3D stresses has no influence on the mechanical design of the system since its Tresca stress is always lower than the ones from the other models at the center of the matter. Another important result highlighted here is that the stress in the hollow disks are 2 times larger than in the solid ones. This directly impacts the reachable speed limit and explains why it is preferable to fasten the rotor to the shaft on both sides rather than to pass it through the center.

Finally, it is important to mention that the stress concentration is the highest at the center of the rotor for all our study cases. As a result, the maximum reachable peripheral speed is mainly limited by the material being closest to the axis of rotation. This is one of the reasons why a high-speed induction motor dedicated to aerospace applications can be made of a solid steel rotor surrounded by a copper conductor ring.

B. *Application to PMSM rotor*

As mentioned above, only the stresses in the sleeve are considered in this study. The proposed analytical models are compared to the expression of stresses given in [1] and finite element simulations performed on ABAQUS. The Finite element models consit in modelling, 1) only the sleeve with an internal pressure and a centrifugal effect, the internal pressure represents the prestress and the centrifugal effect of magnets and rotor yoke. 2) the entire rotor with the mechanical interference between the sleeve and the permanent magnet and also the centrifugal effect.

Geometries are represented in 2D cartesian coordinate system. Regarding the first simulation, only the bandage is studied. It is, modelled as a ring with an inner radius of 63,7 mm. The outer radius depends on the thickness of the sleeve. For glass-fiber, we consider a density of 2,600 kg/m^3, a Young's modulus of 73 GPa and Poisson's ratio of 0.25. The bandage is divided into four parts. As we are in a 2D finite element simulation, among the previously boundaries conditions used in the solid rotor, only x and y conditions are applied. The sleeve is subjected to a rotational body force and an internal pressure symbolizing the prestress. The size of mesh elements is chosen to obtain at least four elements in the thickness of the bandage.

Concerning the second simulation, all the parts of the rotor are represented, but the methodology is the same. Only the materials parameters vary and the prestress is modeled by defining the mechanical interference between the parts. The geometrical and physical parameters are summarized in Table III.

TABLE III
GEOMETRICAL AND PHYSICAL PARAMETERS OF THE MATERIALS

	Steel	Magnet	Bandage
ρ (kg/m^3)	7,800	7,500	2,600
E (GPa)	210	160	73
ϑ	0.3	0.24	0.25
R_{int} (mm)	24.2	56.7	63.7
R_{ext} (mm)	56.7	63.7	63.7+e_f

Fig. 4. shows the different results where one can observe the same evolution trends that are also consistent with the results presented in [1]. It is worth noting that the analytical models well agree with the finite element simulations. It is important to mention that the first analytical model which considers a sleeve in rotation with an internal pressure gives similar results compared to finite element simulations of the bandage alone. The CPU time being much faster (5.6 ms VS 28s), this model is then of great interest for optimization studies. Furthermore, the numerical simulation gives the same results than the displacement method.

Fig. 4. Stress analysis in bandage for a high-speed rotor

Finally, all the models lead to consistent results and in order to ensure the safety of the rotor, we will choose the most pessimistic model to size our sleeve. For a thickness of around 2 mm, the sleeve can resist to the centrifugal effect and the prestress as the elastic resistance of glass-fiber is close to 1,000 MPa.

V. INDUSTRIAL APPLICATION

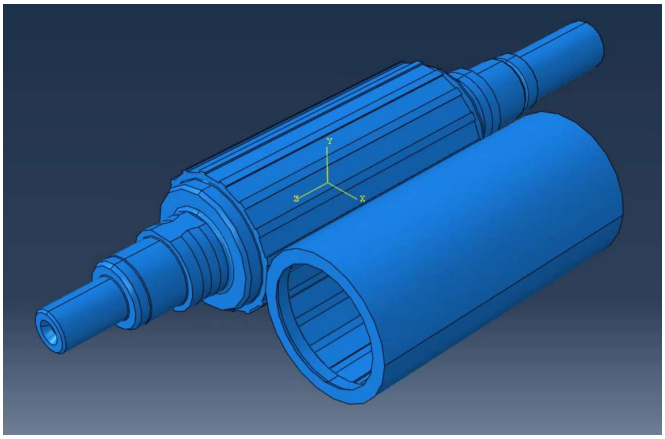
Fig. 5. Bi-layer rotor of an induction machine operating at 36,000 rpm

As shown in III.B. the analytical model considering only a 2D stress depending only on the radial position is enough to dimension the rotor. Thus, one can use this model to verify if a real aircraft rotor of an induction machine is well designed to withstand the centrifugal stress at 46,000 rpm, its rated top speed. As shown in Fig.5. the rotor is composed of one layer of steel which extend itself to 15.4 mm and then a layer of copper to 16.5 mm. The total distance between the shaft extremities is equal to 15 cm. Once again, we compare the analytical model to both 2D and 3D finite element simulations. For the mesh generation and the characterization of the displacements we use the same method described in the previous parts.

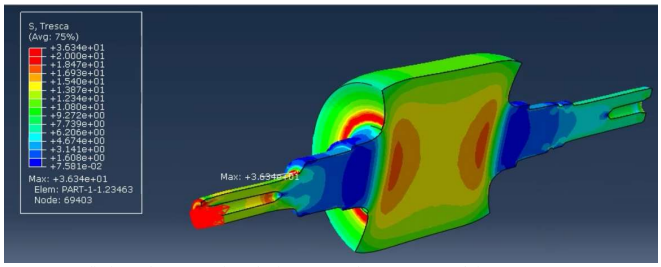

Fig. 6. 3D finite element simulations results computed in ABAQUS. One can see the Tresca constraint in MPa at 46,000 rpm, red and orange areas are for the maximum stress.

Fig. 6. shows that the maximum constraints are located at the extremities of the rotor shaft. Then comes the maximum constraints in the center of the rotor. In order to compare the analytical results to the 2D and 3D finite element simulations, the stress vs. radius curve is plotted in a cross section located in the middle of the rotor, Fig.7.

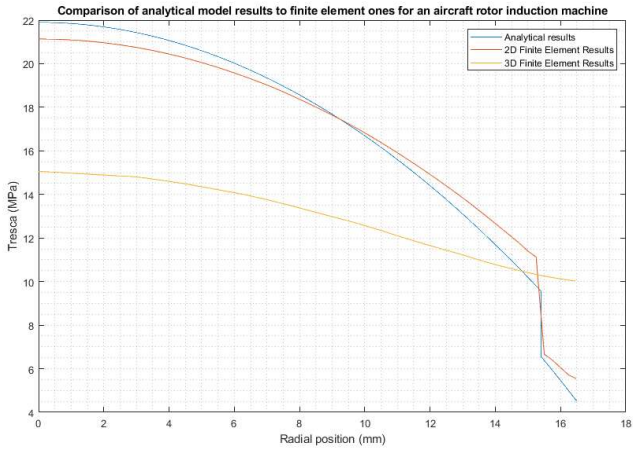

Fig. 7. Results of the comparison in a cross section of the rotor at 46,000 rpm.

Firstly, one can observe that the analytical and the 2D FE models, developed under the same conditions, give very close results. However, the 3D FE model which considers the actual grooved geometry shown in Fig. 5 lead to different results. This is due to surface interactions in the matter which change Tresca criteria value. Moreover, we notice that the 3D computed constraint evolves smoothly while the 2D computations show a Tresca constraint discontinuity at copper-steel interface.

Analytical results overestimate the maximal Tresca constraint issued from the 3D model., Hence, the use of the 2D analytical model remains interesting when repetitive computations are needed during an optimization of this machine.

Finally, all the presented results are far from the limit of 400 MPa and 70 MPa which are respectively yield strength of steel and copper. This may lead to the conclusion that we are still above the speed limit of the rotor but it is not the case. Even if we still have to consider a certain safety factor it will not explain the difference. In fact, this product has been sized including the thermal effects which will be here high as we are considering an induction motor. Thus, Eddy currents will first heat the copper layer and then the steel one. This will lead to a thermal expansion of materials, new values for the mechanical parameters, making the constraints much higher in the rotor.

VI. CONCLUSION

Several 2D and 3D analytical models have been proposed for stress analysis in high-speed rotor machines. Finite element computations allowed us to validate these models. The plane stress 2D models seem to be sufficient to accurately evaluate the constraints in the studied cases. Hence, they can be used with a great confidence during an optimization study where repetitive computations are needed. In fact, the CPU time savings are significant (5,000 time faster) in comparison the numerical evaluations. Solid rotor induction machines and permanent magnets machines have been studied. It has been shown that the solid rotor machine is better suited to high speed than the PMSM since it presents 3 times less stress. Finally, the application on an industrial case study allowed to put forward the great safety factors which are taken to ensure an operation at high-speed levels. In the future, the analytical mechanical models presented here will be coupled, in a multiphysics way, to electromagnetic and thermal analytical models to achieve a quick and robust sizing of the studied machines.

VII. REFERENCES

[1] A. Binder, T. Schneider, et M. Klohr, « Fixation of buried and surface-mounted magnets in high-speed permanent-magnet synchronous machines », IEEE Transactions on Industry Applications, vol. 42, no 4, p. 1031-1037, juill. 2006, doi: 10.1109/TIA.2006.876072.

[2] J. Swanke, D. Bobba, T. M. Jahns, et B. Sarlioglu, « Comparison of Modular PM Propulsion Machines for High Power Density », in 2019 IEEE Transportation Electrification Conference and Expo (ITEC), juin 2019, p. 1-7. doi: 10.1109/ITEC.2019.8790587.

[3] E.-H. Z. M. Abderrezak REZZOUG, M. E.-H. Zaïm, et A. Rezzoug, Machines électriques non conventionnelles. Lavoisier, 2011.

[4] G. Spinnler, « Conception des machines: principes et applications (vol. 3) - Dimensionnement - Georges Spinnler (EAN13 : 9782880743031) », EPFL Press. https://www.epflpress.org/produit/141/9782880743031/conception-des-machines-principes-et-applications-vol-3 (consulté le 26 novembre 2021).

[5] G. Burnand, D. Araujo, et Y. Perriard, « Very-high-speed permanent magnet motors: Mechanical rotor stresses analytical model », mai 2017, p. 1-7. doi: 10.1109/IEMDC.2017.8002066.